Title

Hours-long Near-UV/Optical Emission from Mildly Relativistic Outflows in Black Hole—Neutron Star Mergers

Authors

Gottlieb, Ore
Issa, Danat
Jacquemin-Ide, Jonatan
et al.

Hours-long Near-UV/Optical Emission from Mildly Relativistic Outflows in Black Hole–Neutron Star Mergers

Ore Gottlieb[1] , Danat Issa[1] , Jonatan Jacquemin-Ide[1] , Matthew Liska[2,3] , Alexander Tchekhovskoy[1] , Francois Foucart[4] ,
Daniel Kasen[5,6,7] , Rosalba Perna[8,9] , Eliot Quataert[10] , and Brian D. Metzger[9,11]

[1] Center for Interdisciplinary Exploration & Research in Astrophysics (CIERA), Physics & Astronomy, Northwestern University, Evanston, IL 60202,
USA; oregottlieb@gmail.com
[2] Institute for Theory and Computation, Harvard University, 60 Garden Street, Cambridge, MA 02138, USA
[3] John Harvard Distinguished Science and ITC, USA
[4] Department of Physics and Astronomy, University of New Hampshire, 9 Library Way, Durham, NH 03824, USA
[5] Astronomy Department and Theoretical Astrophysics Center, University of California, Berkeley, Berkeley, CA 94720, USA
[6] Physics Department, University of California, Berkeley, Berkeley, CA 94720, USA
[7] Nuclear Science Division, Lawrence Berkeley National Laboratory, Berkeley, CA 94720, USA
[8] Department of Physics and Astronomy, Stony Brook University, Stony Brook, NY 11794-3800, USA
[9] Center for Computational Astrophysics, Flatiron Institute, New York, NY 10010, USA
[10] Department of Astrophysical Sciences, Princeton University, Princeton, NJ 08544, USA
[11] Department of Physics and Columbia Astrophysics Laboratory, Columbia University, Pupin Hall, New York, NY 10027, USA

Abstract

The ongoing LIGO–Virgo–KAGRA observing run O4 provides an opportunity to discover new multimessenger events, including binary neutron star (BNS) mergers such as GW170817 and the highly anticipated first detection of a multimessenger black hole–neutron star (BH–NS) merger. While BNS mergers were predicted to exhibit early optical emission from mildly relativistic outflows, it has remained uncertain whether the BH–NS merger ejecta provides the conditions for similar signals to emerge. We present the first modeling of early near-ultraviolet/optical emission from mildly relativistic outflows in BH–NS mergers. Adopting optimal binary properties, a mass ratio of $q = 2$, and a rapidly rotating BH, we utilize numerical relativity and general relativistic magnetohydrodynamic (GRMHD) simulations to follow the binary's evolution from premerger to homologous expansion. We use an M1 neutrino transport GRMHD simulation to self-consistently estimate the opacity distribution in the outflows and find a bright near-ultraviolet/optical signal that emerges due to jet-powered cocoon cooling emission, outshining the kilonova emission at early time. The signal peaks at an absolute magnitude of ~ -15 a few hours after the merger, longer than previous estimates, which did not consider the first principles–based jet launching. By late 2024, the Rubin Observatory will have the capability to track the entire signal evolution or detect its peak up to distances of $\gtrsim 1$ Gpc. In 2026, ULTRASAT will conduct all-sky surveys within minutes, detecting some of these events within ~ 200 Mpc. The BH–NS mergers with higher mass ratios or lower BH spins would produce shorter and fainter signals.

Unified Astronomy Thesaurus concepts: Compact binary stars (283); Compact objects (288); Astrophysical black holes (98); Relativistic jets (1390); Jets (870); Gamma-ray bursts (629); Near ultraviolet astronomy (1094); Ultraviolet astronomy (1736); Optical astronomy (1776); Transient sources (1851); Ultraviolet transient sources (1854); Hydrodynamical simulations (767)

1. Introduction

The binary neutron star (BNS) merger GW170817 demonstrated that, in addition to gravitational waves (GWs), BNSs also produce emission throughout the entire electromagnetic spectrum, making them promising multimessenger sources (see Nakar 2020; Margutti & Chornock 2021, for reviews). While black hole (BH) mergers are unlikely to produce any electromagnetic counterparts to GWs (see, however, Perna et al. 2016), the disruption of an NS during a coalescence with a BH may give rise to kilonova emission powered by radioactive decay of heavy r-process elements (e.g., Rosswog 2005; Surman et al. 2008; Metzger et al. 2010a; Tanaka et al. 2014; Fernández et al. 2015, 2017; Foucart et al. 2015; Kawaguchi et al. 2016; Darbha et al. 2021; Wanajo et al. 2022;

Ekanger et al. 2023; Gompertz et al. 2023), making them another potential multimessenger event that can be detected in LIGO–Virgo–KAGRA (LVK) runs. Understanding the electromagnetic emission in BH–NS mergers is of particular interest, since it might be the primary messenger to enable the distinction between BNS and BH–NS mergers, at least for moderate mass ratios of $q \lesssim 3$, high BH spin, and a relatively stiff equation of state (EoS; see, e.g., Tanaka et al. 2014; Yang et al. 2018; Fragione 2021).

Similar to BNS mergers, BH–NS mergers may also harbor relativistic jets that give rise to additional electromagnetic counterparts, such as a short gamma-ray burst (sGRB) and afterglow emission (Paczynski 1991; Mochkovitch et al. 1993; Janka et al. 1999; Etienne et al. 2012; Kiuchi et al. 2015; Paschalidis et al. 2015; Ruiz et al. 2018; Hayashi et al. 2022a, 2022b). Unlike the kilonova signal, which can be observed from various angles, the detection of a GRB relies on the alignment of the jet with our line of sight. The LVK observing run O3 detected at least one BH–NS merger,

GW200115 (with GW200105 being an additional controversial source; Abbott et al. 2021), for which no electromagnetic counterparts were detected (Dichiara et al. 2021; Zhu et al. 2021). Thus, if these mergers powered relativistic jets, the jet prompt emission was beamed away from Earth. Similarly, most future GW detections of BH–NS mergers are expected to fall outside the narrow beaming angle of the jet, making it unlikely to observe a coincident GW–sGRB signal. Nevertheless, the interaction between the jet and the merger ejecta could give rise to a hot, energetic cocoon that produces wide-angle emission. While the presence of ejecta is expected in certain BH–NS merger configurations of mass ratio and premerger BH spin (Shibata & Uryū 2006, 2007; Etienne et al. 2008; Rantsiou et al. 2008; Shibata & Taniguchi 2008, 2011; Duez et al. 2010; Foucart et al. 2011, 2012, 2014, 2017, 2018, 2019; Kyutoku et al. 2011, 2013, 2015, 2018; Foucart 2012; Kawaguchi et al. 2015; Brege et al. 2018; Hayashi et al. 2021; Most et al. 2021), the amount of polar ejecta might not be sufficient to generate an energetic cocoon. Therefore, the role of cocoon emission in BH–NS mergers remains unclear.

The electromagnetic observations of GW170817 provided valuable insights into the cocoon emission, revealing two distinct processes: shock breakout emission in γ/X-rays (Kasliwal et al. 2017; Gottlieb et al. 2018b) and multiband synchrotron emission (e.g., Mooley et al. 2018a, 2018b; Lazzati et al. 2018). Although the electromagnetic data within the first $\sim$10 hr after GW170817 were not available, it is expected that during that period, the cocoon also emitted radiation in the near-UV (NUV)/optical bands through multiple emission mechanisms characterized by two distinct timescales. (i) For $t \lesssim 1$ hr, the emission is attributed to enhanced β-decay of free neutrons (Gottlieb & Loeb 2020) and cooling envelope emission (Metzger et al. 2015; Kasliwal et al. 2017; Nakar & Piran 2017; Gottlieb et al. 2018a; Piro & Kollmeier 2018). (ii) For $t \gtrsim 1$ hr, the dominant processes include boosted radioactive decay of heavy r-process elements (kilonova; Metzger et al. 2015; Kasliwal et al. 2017; Nakar & Piran 2017; Gottlieb et al. 2018a; Piro & Kollmeier 2018; Hamidani & Ioka 2023) and subsequent synchrotron emission from the β-decay electrons (Gottlieb & Loeb 2020). Notably, none of these cocoon signals have been investigated in the context of BH–NS mergers.

In this Letter, we focus on the early NUV/optical emission, which plays a crucial role in constraining various aspects such as the fate of the jet, the distribution and composition of the ejecta, and facilitating follow-up observations (however, the multiple predictions cause difficulties in discriminating the potential signals; see Arcavi 2018; Gottlieb & Loeb 2020). We utilize numerical relativity simulations of the premerger phase, which we subsequently remap onto a general relativistic magneto-hydrodynamic (GRMHD) setup. By evolving the system until the homologous phase, we achieve a self-similar evolution of the outflow. Based on these numerical results, we perform the first calculations of the early NUV/optical emission that are based on the self-consistent evolution of the outflow from the premerger phase. These first estimates of cocoon emission in BH–NS mergers serve as valuable insights for potential detection in the LVK observing runs O4 and/or O5.

2. Calculation Method

We build on a numerical relativity simulation in SpEC (SpEC Collaboration 2023) that evolves the premerger to 8 ms

Table 1
A Summary of the Models' Parameters.

Model	A	β_p	t_f (s)	$M_{\rm ej}$ (10^{-2} $M_\odot$)	t_b (s)
H_0	$A = 0$	⋯	8	3	⋯
P_w	$A_\phi \propto \rho^2 r^3$	1000	5	3	0.3
P_c	$A_\phi \propto \rho$	1000	5	3	0.1
P_s	$A_\phi \propto \rho$	100	1.8	5	0.05
T_s	$A_\theta \propto \rho$	1	4	4	4

Note. The model names stand for hydrodynamic (H), poloidal (P), or toroidal (T) initial magnetic fields, and the subscripts indicate the strength of the field: zero (0), weak (w), canonical (c), or strong (s). Here A is the vector potential, β_p is the characteristic gas-to-magnetic pressure ratio, t_f is the final time of the simulation with respect to the merger, $M_{\rm ej}$ is the amount of unbound ejecta at the homologous phase, and t_b is the breakout time of the relativistic outflow from the disk winds.

postmerger. The premerger setup is an aligned system of BHs–NSs, where the BH mass and dimensionless spin are $M_{\rm BH,i} = 2.7$ $M_\odot$ and $a_i = 0.6$, respectively, and the NS mass is $M_{\rm NS} = 1.35$ $M_\odot$. The postmerger BH mass and spin are $M_{\rm BH,f} = 3.8$ $M_\odot$ and $a_f = 0.86$. At 8 ms after the merger, we remap the numerical relativity output to 3D GRMHD simulations using the code H-AMR (Liska et al. 2022). We consider five postmerger magnetic field configurations, where the magnetic field depends on the mass density distribution at the time of remapping, with a cutoff at 5×10^{-4} of the maximum density. The maximum asymptotic Lorentz factor of the jets is set by the initial magnetization of the jets, which in turn is set by the floor values of the simulations, to be $\sigma_0 = 150$. Table 1 summarizes the different magnetic configurations considered in the post-merger evolution. The full details of the simulation are given in a companion paper, Gottlieb et al. (2023).

We evolve the system for several seconds postmerger such that a significant fraction of the outflow has reached homologous expansion. Then, we postprocess the final snapshot of each simulation to semianalytically calculate the predicted NUV and optical emission in the first hours after the merger. We consider adiabatic cooling emission and radioactive decay of heavy r-process elements from sub- and mildly relativistic outflows. Thus, we ignore contributions from elements with a Lorentz factor $\gamma > 4$, which have yet to reach their asymptotic velocity, and consider only elements far enough from the jet axis, $\theta > 12°$, where the cocoon maintains a self-similar structure as it evolves. Therefore, our calculation is in fact a lower limit on the cocoon emission.

The full description of the semianalytic calculation is given in Appendix. Here we summarize the main steps. At each line of sight, we consider only the gas that is homologous at this time; namely, the radial velocity component dominates and scales as $v \sim v_r \propto r$ (most of the main ejecta does not). The top panel of Figure 1 demonstrates that the homologous expansion begins at $r \gtrsim 10^{9.5}$ cm at most angles far from the jet opening angle. At $\theta = 10°$ (blue), the flow is nonhomologous at all radii due to the abrupt and turbulent jet structure. Using the radial profile, we extrapolate the gas evolution adiabatically (before it becomes radiative) to later times.

To self-consistently evolve the ejecta composition, which is probed by the electron fraction, Y_e, we run an additional postmerger simulation that is identical to model P_c but employs the Helmholtz EoS and neutrino physics using M1 neutrino transport. The Helmholtz EoS (Timmes & Swesty 2000) is implemented in a tabulated form in ($\log \rho$, $\log T$, Y_e) and
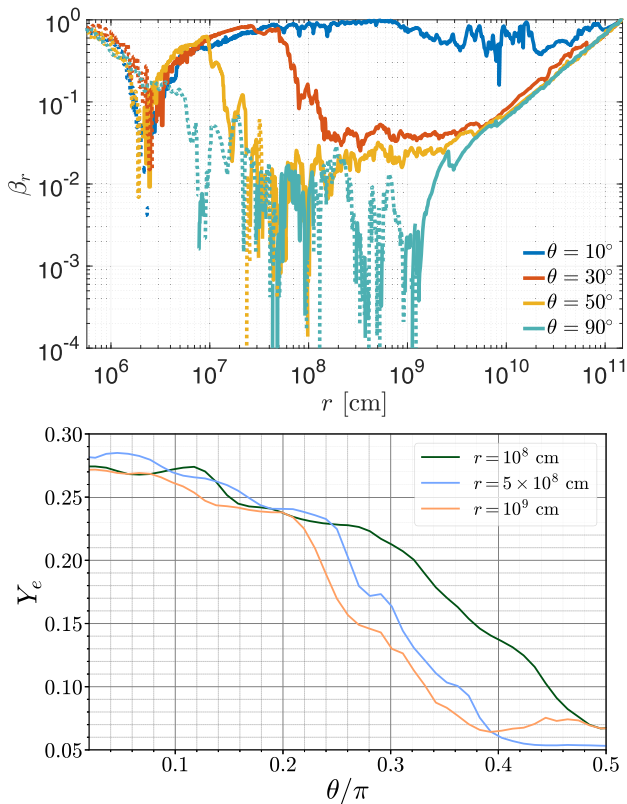
Figure 1. Top: dimensionless velocity profile at various polar angles, measured at $\phi = 0$. Solid (dotted) lines represent outflows (inflows). Homologous material ($v \propto r$) is seen at $r \gtrsim 10^{9.5}$ cm at most angles $\theta \gtrsim 20°$. Around the jet (blue), the radial velocity profile is stochastic. Bottom: ϕ-averaged Y_e as a function of the polar angle at different radii, calculated from a BH–NS postmerger simulation with the M1 scheme, measured 0.15 s after the merger.

includes the contributions of the ideal gas of ions, radiation, and degenerate pressure of the electron–positron plasma. Neutrino transport is implemented similar to Foucart et al. (2015, 2016), with the neutrino weak force interactions included via table interpolation using NuLib (O'Connor 2015). This simulation evolves for 0.15 s postmerger, while the jet is launched within the first 0.01 s after the merger in this model. The grid resolution is $128 \times 96 \times 96$ cells. Using this simulation, we find the electron fraction distribution in the jet and disk winds to estimate $\kappa(\theta)$ through the dependency on Y_e (see, e.g., Tanaka et al. 2020).

The bottom panel of Figure 1 depicts the ϕ-averaged electron fraction as a function of the polar angle 0.15 s after the merger. It shows a moderate electron fraction $Y_e \approx 0.25$ at the jet–cocoon angles, $\theta \lesssim 45°$, which gradually drops to $Y_e \lesssim 0.1$ at $\theta \gtrsim 70°$. We find only a weak dependence of the electron fraction on the distance from the BH and the azimuthal angle. Thus, we use $Y_e(\theta)$ to estimate the angle-dependent gray opacity $\kappa(Y_e)$, as fitted by Wu et al. (2022) and consistent with Tanaka et al. (2020):

$$\kappa(\theta) = 1 + \frac{9}{1 + [4 Y_e(\theta)]^{12}} \frac{\text{cm}^2}{\text{g}}. \quad (1)$$

We emphasize that the remapping of Y_e to κ assumes a narrow range of temperatures of several thousand kelvins. During the first hour, the cocoon temperature is $T \gg 10^4$ K, for which the r-process opacities in the literature are only partly understood. Recent radiative transfer simulations that estimated the opacity

in the range $10^4 \text{ K} \lesssim T \lesssim 10^5$ K indicate that the opacity values of high Y_e at this temperature range might be somewhat lower than in Equation (1) (see Figure 7 in Banerjee et al. 2020), but this highly depends on the atomic composition (Banerjee et al. 2023). Therefore, we also examine the case of constant $\kappa = 1 \text{ cm}^2 \text{ g}^{-1}$ for comparison. In the other extreme regime of $T \lesssim 3000$ K, lanthanide recombination takes place and the r-process opacity falls dramatically (Kasen et al. 2013), but these temperatures are only of concern at later times than those studied here. Using $\kappa(\theta)$, we calculate the radial optical depth assuming the photons diffuse radially[12] (Equation (A1)). We find the trapping radius and photosphere along each line of sight and for each time.

At each time and line of sight, we calculate the local luminosity at the trapping radius and the temperature at the photosphere using the Stefan–Boltzmann law, assuming blackbody locally. We consider two emission contributions: (i) r-process emission L_r (Equation (A4)) due to radioactive heating from β and γ decay in the gas outside the trapping radius in a comoving rate $\dot{Q}(t) \sim t^{-1.3}$ (e.g., Metzger et al. 2010b) and (ii) cooling emission L_c (Equation (A2)) from the thermal energy of the gas and β and γ radioactive heating inside the trapping radius. Finally, we boost the bolometric and spectral luminosities to the observer frame and integrate the emission over all angles and equal light travel times.

3. Outflow Evolution and Emission

When the initial magnetic configuration in the disk is of a strong poloidal field, the jet power of $\sim 10^{52} \text{ erg s}^{-1}$ is considerably higher than that of typical sGRBs. In all other models, the jet power is 10^{50}–$10^{51} \text{ erg s}^{-1}$, consistent with typical sGRBs. However, in these cases, the jet operates for several seconds, exceeding the characteristic subsecond duration of sGRBs but consistent with long-duration sGRBs (e.g., Rastinejad et al. 2022). When the initial field is toroidal, the jet can only be launched once the dynamo process generates a global poloidal field after ~ 1 s. Regardless of the specific magnetic configuration, turbulence in the disk releases quasi-isotropic massive winds (Table 1) during the first ~ 1 s after the merger (Gottlieb et al. 2023).

The interaction between the winds and jets generates a mildly relativistic hot cocoon, which is composed of shocked jet and shocked wind material, at the expense of jet power. This implies that forming a cocoon does not necessitate dynamical ejecta. Thus, cocoons accompany all jets, given that jets require an accretion disk that launches winds. Figure 2 depicts 3D renderings of the four models with magnetic fields that generate relativistic outflows, taken at $t = t_f$. Along the equatorial region, low Y_e winds (red) from the disk (yellow) are shocked by the relativistic jet (light blue) along the polar axis, resulting in the formation of a massive, hot cocoon (dark blue) surrounding the jet. The cocoon, consisting of r-process elements, emits both radioactive heating emission and cooling emission due to its adiabatic expansion.

---

[12] Deviations from sphericity were found to be important during the early BH–NS postmerger, which exhibits a quasi-planar structure such that photons leak nonradially (Kawaguchi et al. 2016; Darbha & Kasen 2020; Darbha et al. 2021). However, when relativistic outflows are present, a more isotropic expanding gas structure is obtained (Figure 2) so that the radial diffusion approximation is reasonable.
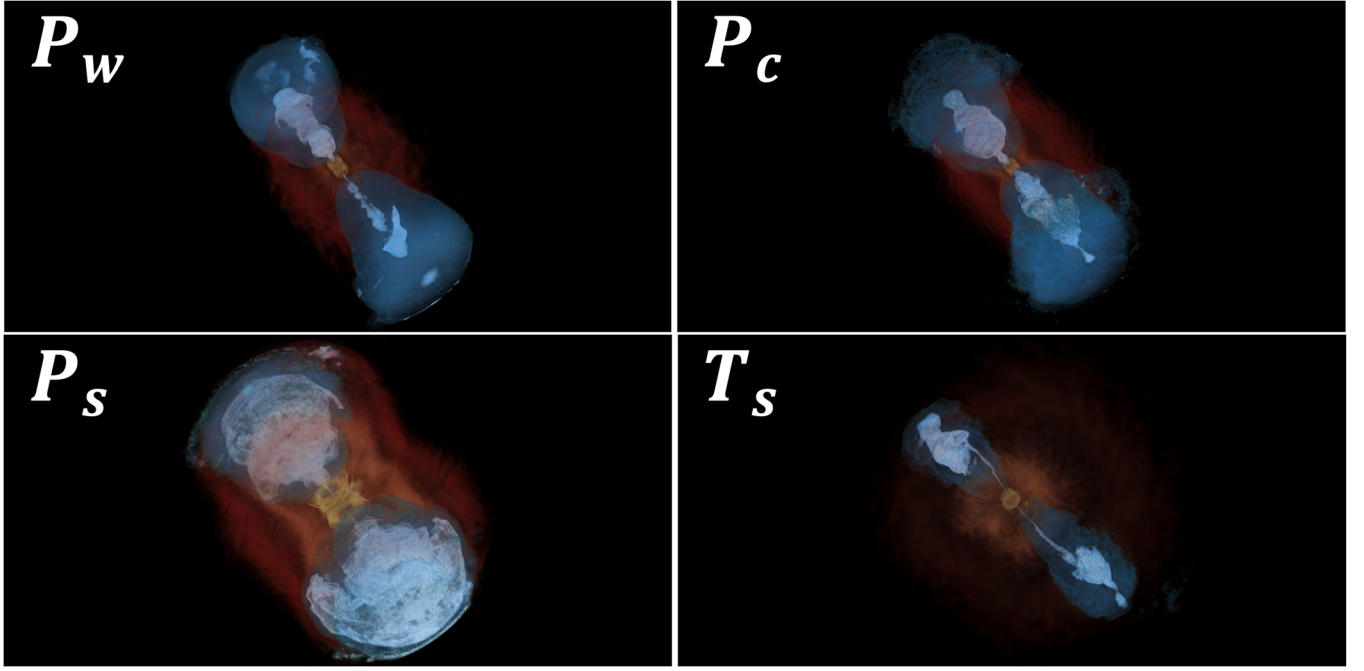
Figure 2. The 3D renderings of the final snapshot of each simulation. The outflows in the poloidal field configurations reach $r \approx c t_f$, and in model T_s, the outflow front is at $r = 8.8 \times 10^{10}$ cm. The blue parts display the asymptotic proper velocity, showing the sub- and mildly relativistic cocoon (dark) enveloping the relativistic jets (light). The red and yellow components portray the mass density, showing the merger ejecta and the accretion disk components, respectively. See full movies of models T_s and P_c at http://www.oregottlieb.com/bhns.html.

Using a characteristic cocoon mass of $M \approx 10^{-3}\, M_\odot$ and proper velocity of $\beta \approx 0.7$, the observed emission peaks on a timescale given by Equation (A9):

$$t_{\rm obs} \approx \left[\frac{\kappa M \gamma}{4 {\rm vc}} \left(1 - \frac{v}{c} \right)^3 \right]^{0.5}$$

$$\approx 3 \left(\frac{\kappa}{5\ {\rm cm^2\ gr^{-1}}} \frac{M}{10^{-3} M_\odot} \frac{\left(\frac{1-\beta}{0.3} \right)^3}{\frac{\beta}{0.7}} \right)^{0.5} {\rm hr}. \qquad (2)$$

The emission profile is expected to vary with the viewing angle due to differences in opacity (characterized by Y_e), mass, and velocity. Lighter, faster, and higher Y_e ejecta along the polar axis enables earlier diffusion of photons, which reduces adiabatic losses and leads to an earlier and brighter peak.

Figure 3 depicts the emission profiles averaged over azimuthal angles[13] as a function of the observer time. The first row shows the bolometric luminosity for different models and at various angles, while the lower panels present the light curves in absolute (left y-axis) and apparent at 200 Mpc (right y-axis) magnitudes in the g band (second row), various bands for model P_w (third row), and at different angles in the g band (fourth row). The light-curve evolution can be described by two phases: optically thick and optically thin cocoon.[14]

1. During the first minutes to an hour, the cocoon is still optically thick, and the emission is dominated by the front of the ejecta close to the equator. The strong initial fields in models T_s and P_s result in early ejection of a larger mass, leading to brighter emission. However, despite the high bolometric luminosity at early times (first row), the observed NUV/optical emission is still weak in all models (second row). This is because the color temperature is $T \gtrsim 10^5$ K, causing most of the radiation to exist as X-rays and far-UV photons. Furthermore, these photons cannot diffuse out to the observer due to the high opacity resulting from bound–free transitions (Metzger 2019). This is not taken into account in our calculation; thus, our calculation at early times is inapplicable. Similarly, the validity of the predicted early cocoon-powered X-ray emission proposed by Lazzati et al. (2017a, 2017b) and Hamidani & Ioka (2023) is also called into question.

2. As the cocoon becomes optically thin, a hump appears in the light curve, indicating the release of a significant amount of internal energy leaking out as NUV/optical photons. A clear trend of earlier (Equation (2)) and brighter emission at smaller viewing angles is apparent (top left panel), owing to lighter and more energetic gas close to the jet axis. As the temperature decreases, the NUV/optical light curve rises on a timescale of $t_{\rm obs} \gtrsim 1$ hr. Subsequently, the temperature stabilizes around $T \approx 5 \times 10^3$ K after a few hours, leading to a nearly monochromatic peak in the light curve (third row). As the emission is in the Rayleigh–Jeans regime, the light curves $L_\nu \sim L T^{-3}$ dictate that a constant temperature results in a rapid decline of the light curve with the bolometric luminosity. During the decay in the light curve, the emitting gas is subrelativistic, resulting in nearly isotropic emission (fourth row). Once the absolute magnitude drops below $M_{\rm AB} \approx -13$ at $t_{\rm obs} \approx 10$ hr, the main kilonova signal becomes the dominant source of emission (see, e.g., Gompertz et al. 2023). We do not incorporate the main kilonova component of the ejecta emission, as the slower parts of the ejecta have yet to reach homologous expansion at the time of the final simulation

---

[13] We find negligible variation in the observed light curves when considering different azimuthal angles. However, near the equator, where the emission is predominantly influenced by outflows from the disk, some asymmetry, such as in the tidal tail, leads to variations of up to half a magnitude. At $|\theta_{\rm obs}| \lesssim 60°$, the differences are up to ∼0.2 mag.

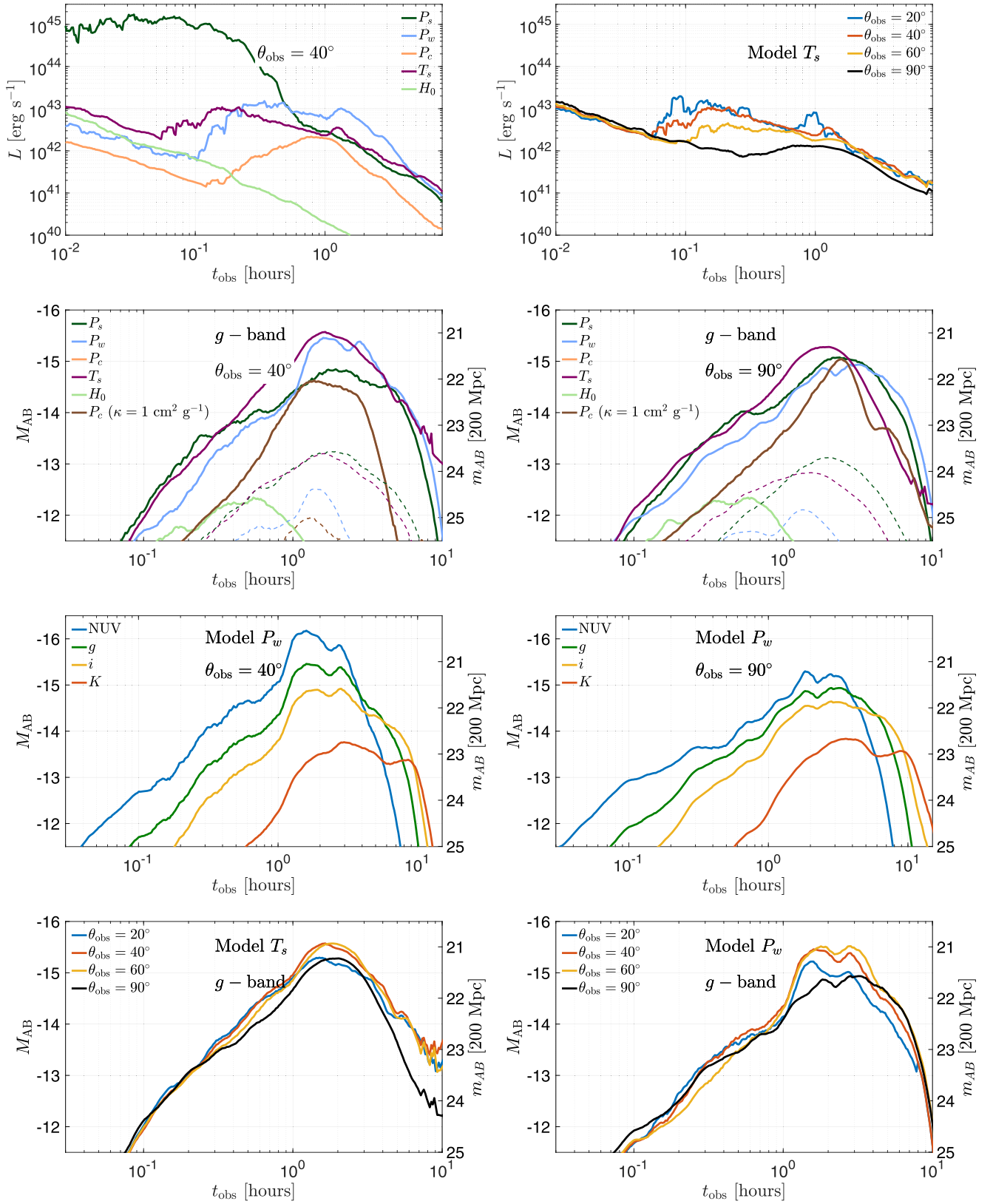[14] Except for model H_0, where there is no cocoon, so only the first phase is present.

Figure 3. First row: bolometric luminosity in different models at $\theta_{\rm obs} = 40°$ (left) and at various viewing angles in model T_s (right). Second row: g-band magnitude ($\lambda = 475$ nm) of different models at $\theta_{\rm obs} = 40°$ (left) and $\theta_{\rm obs} = 90°$ (right). Thin dashed lines represent the contribution of r-process heating outside of the trapping radius. Third row: NUV ($\lambda_{\rm NUV} = 250$ nm), g ($\lambda_g = 475$ nm), i ($\lambda_i = 760$ nm), and K ($\lambda_K = 2160$ nm) bands for model P_w at $\theta_{\rm obs} = 40°$ (left) and $\theta_{\rm obs} = 90°$ (right). Fourth row: different angles in the g band for model T_s (left) and P_w (right). The light curves are shown in absolute magnitude (left y-axis) and apparent magnitude at 200 Mpc (right y-axis).

snapshots. Therefore, our calculations would no longer be valid beyond that point.

The second row of Figure 3 demonstrates that the bright and long cooling emission (thick solid lines) outshines the negligible contribution of radioactive decay emission in the cocoon (thin dashed lines), i.e., $L_r \ll L_c$, at all times. This finding differs from the results of Gottlieb et al. (2018a) and Gottlieb & Loeb (2020), who found a shorter signal and a double-humped structure when $\kappa \lesssim 1 \, \mathrm{cm^2 \, gr^{-1}}$, attributing it to an early cooling signal followed by the kilonova emission from the cocoon. The disparities between our findings and theirs are attributed to two main factors. First, the angular distribution of the electron fraction indicates that although the opacity is uncertain at these high temperatures, it seems to be relatively high, $\kappa \gtrsim 5 \, \mathrm{cm^2 \, g^{-1}}$, resulting in a rather faint kilonova signal, akin to their models with $\kappa = 10 \, \mathrm{cm^2 \, g^{-1}}$. Indeed, when $\kappa = 1 \, \mathrm{cm^2 \, g^{-1}}$ (brown lines), the cooling emission peaks at half the time (see also Equation (1)); however, it still outshines the radioactive decay heating. Second, whereas they found the cocoon to contain only 10% of the jet energy, our cocoons have a comparable energy to the jets and thus are an order of magnitude more massive. This is due to either more powerful outflows that unbind a larger amount of ejecta (e.g., model P_s) or the late activation of a magnetically arrested disk (e.g., models T_s, P_s, and P_w) that prolongs the interaction between the jet and the ejecta. The cocoon–jet energy ratio depends on the amount of ejecta, among other things, which in turn depends on the binary properties. These factors could not be addressed in previous models, as the self-consistent modeling of jet launching was absent. An order-of-magnitude more massive cocoon explains why the signal is ∼three times longer (Equation (2)). We note that both of these aspects may be altered in other binary merger configurations, where the jet is likely less energetic (see Gottlieb et al. 2023), or when neutrinos are incorporated into the postmerger simulation, as neutrino cooling influences both the electron fraction and the amount of unbound ejecta (see Section 4).

Our results suggest that BH–NS mergers with the specific properties examined in this study are expected to be accompanied by an NUV/optical signal peaking at an apparent magnitude of ∼21–22 in the UV/g band at the detection horizon of LVK run O4, $D \approx 200$ Mpc (Abbott et al. 2020). This magnitude makes the peak of closer events detectable by the Zwicky Transient Facility (ZTF; Graham et al. 2019; Dekany et al. 2020) at some viewing angles. Future telescopes such as the Rubin Observatory (LSST Science Collaboration et al. 2009) and ULTRASAT (Ben-Ami et al. 2022; Shvartzvald et al. 2023) are projected to survey the sky down to single-visit magnitudes of ∼25 and ∼22, respectively. Rapid wide-field follow-up observations in the NUV and optical ranges, triggered by a GW detection from a BH–NS merger, could successfully detect these electromagnetic signals. Rubin Observatory will have the capacity to monitor the evolution of such signals within the LVK O4 detection horizon or detect parts of them at distances of $D \gtrsim 1$ Gpc.

4. Discussion

We conducted the first calculation of early NUV/optical emission originating from relativistic outflows that evolve self-consistently in compact binary mergers starting from the premerger phase. Notably, this is the first computation of such emission specifically in the context of BH–NS mergers and the

first to utilize M1 neutrino transport in large-scale jets. Our investigation involved tracking the evolution of an aligned BH–NS binary with a mass ratio of $q = 2$ and a BH dimensionless spin of $a = 0.6$, starting from the premerger and progressing to the homologous expansion. Subsequently, we advanced the system semianalytically to the emission zone. By considering cooling envelope and r-process radioactive decay emission mechanisms, we calculated the light curves in the NUV/optical bands for different outflows and at various viewing angles.

Our findings indicate that in BH–NS mergers with low mass ratios and high BH spin, the presence of relativistic jets leads to a bright NUV/optical signal that lasts for a few hours. This signal peaks at an absolute magnitude of $M_{AB} \approx -15$, outshining any contribution from radioactive decay emission. Compared to previous studies of cocoon cooling emission that did not incorporate self-consistent jet launching, our results demonstrate a longer-lasting signal, owing to a more accurate estimation of the cocoon energy resulting from the interaction between the jet and ejecta.

The brightness of these signals may enable their detection by the ZTF out to ∼100 Mpc. The upcoming Rubin Observatory, scheduled to begin observations during the later stages of O4, will be capable of effectively monitoring the entire evolution of such signals and detecting parts of them at distances beyond $D \gtrsim 1$ Gpc. Additionally, ULTRASAT, anticipated to launch in 2026, will cover the entire sky within minutes, enabling the detection of some of these signals out to ∼200 Mpc.

Detecting and interpreting the signals from these outflows poses a crucial question: what insights can we gain about the system? Differentiating between various types of outflows is a highly challenging task due to the complex and nonlinear nature of their evolution, as well as the inherent degeneracy in the system properties. The brightness of the signals is influenced by the strength of the outflows, the viewing angle, and the optical depth of the outflow. We do not find any clear signature of the outflow structure or the initial magnetic field configuration in the light curves.

Another question to consider is whether we can distinguish BH–NS mergers from BNS mergers. Inferring the merger type based on the early emission from BH–NS mergers with a mass ratio of $q = 2$ may be unfeasible, as such systems might evolve in a similar way to BNS mergers if the BNS merger product collapses to a BH relatively fast. However, BH–NS mergers can manifest in various forms with lower BH spins, higher mass ratios, and misaligned orbits. These variations lead to less mass remaining outside the BH innermost stable circular orbit after the merger, resulting in a reduced energy reservoir for jet launching and disk winds and, subsequently, a less energetic cocoon.

In the companion paper, Gottlieb et al. (2023), we show that all jets exhibit either excessive luminosity or an extended launching process when compared to typical sGRBs. The reason behind this lies in the fact that, in order to achieve the expected luminosity of sGRBs, the jets must reach their maximum efficiency after a significant decrease in the accretion rate. However, this necessitates a longer duration for the jet launching process than what is typically observed in sGRBs. This poses a fundamental challenge to our current understanding of jet formation in binary mergers. A possible solution is that most sGRB jets in these binaries are launched from low premerger BH spin, as suggested by LVK observations (Abbott et al. 2021), or in higher mass ratio and spin–orbit

misaligned binaries, as suggested by population synthesis models (Belczynski et al. 2008). In all such cases, the bound mass (disk) will be lower, such that the jet and cocoon (emission) will be weaker. Therefore, the aforementioned variations in the merger properties might be favored in order to fit sGRB observations. Thus, while a low mass ratio is similar to BNS mergers and ideal for cocoon emission, other BH–NS mergers might exhibit considerably earlier, shorter, and fainter emission, which could display distinct characteristics compared to BNS mergers.

An alternative method for deducing the nature of the system is to examine observational signatures that are exclusive to each merger type. For example, the role of the cocoon's kilonova, as previously proposed in Nakar & Piran (2017), Gottlieb et al. (2018a), Gottlieb & Loeb (2020), and Hamidani & Ioka (2023), remains uncertain, as we find here, and due to the considerable reliance on the poorly understood opacity of the hot cocoon, it might differ between BNS and BH–NS mergers. Additionally, if a fast tail of free neutrons is unique to BNS mergers, it could aid in identifying the merger type. This could be achieved through the detection of radioactive decay emission from free neutrons in the ejecta (Metzger et al. 2015) or within the cocoon (Gottlieb & Loeb 2020), although its emission likely overlaps with other mechanisms occurring on a similar timescale. Finally, when the cocoon breaks free from the ejecta, γ-ray photons leak out through the breakout layer, generating a short-lived shock breakout signal, the characteristics of which strongly depend on the front ejecta mass and velocity (Gottlieb et al. 2018b). The BH–NS mergers might exhibit a different front ejecta structure compared to BNS mergers, providing yet another electromagnetic counterpart that could aid in identifying the merger type. Calculation and comparison of the shock breakout emission in various merger configurations is a topic for future work.

To address the challenges mentioned above, we plan to (i) conduct a comprehensive analysis spanning from premerger to postmerger stages of BH–NS systems with higher mass ratios and lower BH spins; (ii) perform a self-consistent radiative transfer calculation of the emission in order to properly resolve physical processes such as ionization of the material near the photosphere, reprocessing of photons, and nonradial photon diffusion (Darbha & Kasen 2020; Darbha et al. 2021); and (iii) employ a complete neutrino transport scheme, which will enable us to properly account for the evolution of neutrinos within the system. We anticipate that neutrino cooling will suppress the early strong winds, leading to a reduction in wind emission and a decrease in the mass of the cocoon. As a result, the cocoon emission will also be attenuated. However, in Gottlieb et al. (2023), we demonstrate that the winds are strongly influenced by magnetized outflows, indicating that they may not be significantly affected by neutrino cooling. The inclusion of neutrino transport will also allow us to self-consistently examine the evolution of the electron fraction within the cocoon. This will enable a more precise calculation of the resulting emission, improving the accuracy of our predictions.

Data Availability

The data underlying this paper will be shared upon reasonable request to the corresponding author.

Appendix
Light-curve Calculation

At time $t = t_f -$ the end of the simulations, most of the outflow reaches homologous expansion. This enables us to advance the outflow expansion in postprocessing using the adiabatic relations. We note that because we do not consider emission from the jet, we can safely ignore the magnetic component, which is negligible outside of the jet. The emission calculation is performed on the unbound 3D outflow as follows. At each line of sight and time, we find the photosphere $R_{ph}(t, \theta, \phi) = R[\tau(t, R_{ph}, \theta, \phi) = 1]$ and the trapping radius $R_{tr}(t, \theta, \phi) = R[\tau(t, R_{tr}, \theta, \phi) = c/v(t_f, R_{tr}, \theta, \phi)]$, where v is the velocity, and τ is the optical depth along a radial line of sight,

$$
\tau(t, r, \theta, \phi) = \left(\frac{t}{t_f}\right)^{-2} \int_r^\infty \kappa(\theta) \rho
$$
$$
\times (t_f, r', \theta, \phi)(1 - v(t_f, r', \theta, \phi)/c)\gamma(t_f, r', \theta, \phi)\mathrm{d}r', \tag{A1}
$$

where ρ is the mass density.

The photons diffuse out from the trapping radius, such that the luminosity per solid angle in the lab frame due to cooling

emission is

$$
\begin{aligned}
L_c(t, \theta, \phi) = & [4p(t_f, R_{\mathrm{tr}}, \theta, \phi) \\
& + AQ(t, r, \theta, \phi)\rho(t, r, \theta, \phi)]\gamma(t_f, R_{\mathrm{tr}}, \theta, \phi)^2 \\
& \times \left(\frac{t_f}{t}\right)^4 v(t_f, R_{\mathrm{tr}}, \theta, \phi) R_{\mathrm{tr}}(t, \theta, \phi)^2,
\end{aligned}
$$
(A2)

where p is the thermal pressure, γ is the Lorentz factor, and the heating rate contribution to cooling due to β and γ radioactive decay is (Hotokezaka et al. 2016)

$$
\begin{aligned}
A &= 1 - \exp\left[-\left(\frac{\gamma(t, r, \theta, \phi)}{t_d}\right)^2\right] + 0.5; \quad \dot{Q}(t, r, \theta, \phi) \\
&= 10^{10}\left[\frac{t_d}{\gamma(t, r, \theta, \phi)}\right]^{-1.3} \frac{\mathrm{erg}}{\mathrm{g\,s}}
\end{aligned}
$$
(A3)

and may vary with the composition to within a factor of a few (see, e.g., Freiburghaus et al. 1999; Metzger et al. 2010b; Korobkin et al. 2012; Wanajo et al. 2014; Hotokezaka et al. 2016). The time t_d is defined as $t_d \equiv t/\mathrm{day}$. The first term in Equation (A2) is the adiabatic cooling of the shocked cocoon, as obtained from the radial flux component of the stress-energy tensor. The second term accounts for the radioactive heating of the gas. Both contributions are calculated in the comoving frame and then boosted to the lab frame. The luminosity per solid angle due to radioactive decay in the lab frame is

$$
\begin{aligned}
&L_r(t, \theta, \phi) \\
&= \int_{R_{\mathrm{tr}}}^{\infty} A\dot{Q}(t, r, \theta, \phi)\rho(t, r, \theta, \phi)\gamma(t, r, \theta, \phi)^2 r^2 \mathrm{d}r.
\end{aligned}
$$
(A4)

The total local luminosity is the sum of both contributions, $L(t, \theta, \phi) = L_c(t, \theta, \phi) + L_r(t, \theta, \phi)$. The local temperature is calculated at the photosphere and assumed to be blackbody.

To transform the emission from the lab frame luminosity to the observed frame ($\theta_{\mathrm{obs}}, \phi_{\mathrm{obs}}$), we find

$$
t_{\mathrm{obs}}(\theta, \phi) = t[1 - v(t_f, R_{\mathrm{tr}}, \theta, \phi)/c\mu(\theta_{\mathrm{obs}}, \phi_{\mathrm{obs}}\theta, \phi)],
$$
(A5)

where

$$
\mu(\theta_{\mathrm{obs}}, \phi_{\mathrm{obs}}, \theta, \phi) = \cos\theta\cos\theta_{\mathrm{obs}} + \sin\theta_{\mathrm{obs}}\sin\theta\cos(\phi - \phi_{\mathrm{obs}}).
$$
(A6)

Then, the observed luminosity is

$$
\begin{aligned}
&L_{\mathrm{obs}}(t_{\mathrm{obs}}, R_{\mathrm{tr}}, \theta_{\mathrm{obs}}, \phi_{\mathrm{obs}}) \\
&= \int_0^\pi \int_0^{2\pi} D(t_{\mathrm{obs}}, R_{\mathrm{tr}}, \theta, \phi)^4 \gamma(t_{\mathrm{obs}}, R_{\mathrm{tr}}, \theta, \phi) L(t_{\mathrm{obs}}, \theta, \phi) \mathrm{d}\mu(\theta_{\mathrm{obs}}, \phi_{\mathrm{obs}}, \theta, \phi),
\end{aligned}
$$
(A7)

where $D(t_{\mathrm{obs}}, R_{\mathrm{tr}}, \theta_{\mathrm{obs}}, \phi_{\mathrm{obs}}) = [\gamma(t_{\mathrm{obs}}, R_{\mathrm{tr}}, \theta_{\mathrm{obs}}, \phi_{\mathrm{obs}})(1 - v(t_{\mathrm{obs}}, R_{\mathrm{tr}}, \theta_{\mathrm{obs}}, \phi_{\mathrm{obs}}))]^{-1}$ is the Doppler factor of the emitting gas.
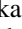
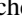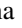The emission peak time is derived as follows. The photons diffuse out from the trapping radius, $\tau(R_{\mathrm{tr}}) = c/v$; thus, Equation (A1) dictates

$$
\frac{3M\kappa}{4\pi(vt)^2}\gamma(1 - v/c) \approx \frac{c}{v}.
$$
(A8)

Approximating Equation (A5) to $t_{\mathrm{obs}} \approx t(1 - v/c)$, we find

$$
t_{\mathrm{obs}} \approx \left[\frac{\kappa M\gamma}{4vc}\left(1 - \frac{v}{c}\right)^3\right]^{0.5}.
$$
(A9)

ORCID iDs

Ore Gottlieb ⓘ https://orcid.org/0000-0003-3115-2456
Danat Issa ⓘ https://orcid.org/0009-0005-2478-7631
Jonatan Jacquemin-Ide ⓘ https://orcid.org/0000-0003-2982-0005
Matthew Liska ⓘ https://orcid.org/0000-0003-4475-9345
Alexander Tchekhovskoy ⓘ https://orcid.org/0000-0002-9182-2047
Francois Foucart ⓘ https://orcid.org/0000-0003-4617-4738
Daniel Kasen ⓘ https://orcid.org/0000-0002-5981-1022
Rosalba Perna ⓘ https://orcid.org/0000-0002-3635-5677
Eliot Quataert ⓘ https://orcid.org/0000-0001-9185-5044
Brian D. Metzger ⓘ https://orcid.org/0000-0002-4670-7509

References

Abbott, B. P., Abbott, R., Abbott, T. D., et al. 2020, LRR, 23, 3
Abbott, R., Abbott, T. D., Abraham, S., et al. 2021, ApJL, 915, L5
Arcavi, I. 2018, ApJL, 855, L23
Banerjee, S., Tanaka, M., Kato, D., & Gaigalas, G. 2023, arXiv:2304.05810
Banerjee, S., Tanaka, M., Kawaguchi, K., Kato, D., & Gaigalas, G. 2020, ApJ, 901, 29
Belczynski, K., Taam, R. E., Rantsiou, E., & van der Sluys, M. 2008, ApJ, 682, 474
Ben-Ami, S., Shvartzvald, Y., Waxman, E., et al. 2022, Proc. SPIE, 12181, 1218105
Brege, W., Duez, M. D., Foucart, F., et al. 2018, PhRvD, 98, 063009
Darbha, S., & Kasen, D. 2020, ApJ, 897, 150
Darbha, S., Kasen, D., Foucart, F., & Price, D. J. 2021, ApJ, 915, 69
Dekany, R., Smith, R. M., Riddle, R., et al. 2020, PASP, 132, 038001
Dichiara, S., Becerra, R. L., Chase, E. A., et al. 2021, ApJL, 923, L32
Duez, M. D., Foucart, F., Kidder, L. E., Ott, C. D., & Teukolsky, S. A. 2010, CQGra, 27, 114106
Ekanger, N., Bhattacharya, M., & Horiuchi, S. 2023, MNRAS, Advance Access
Etienne, Z. B., Faber, J. A., Liu, Y. T., et al. 2008, PhRvD, 77, 084002
Etienne, Z. B., Paschalidis, V., & Shapiro, S. L. 2012, PhRvD, 86, 084026
Fernández, R., Foucart, F., Kasen, D., et al. 2017, CQGra, 34, 154001
Fernández, R., Quataert, E., Schwab, J., Kasen, D., & Rosswog, S. 2015, MNRAS, 449, 390
Foucart, F. 2012, PhRvD, 86, 124007
Foucart, F., Deaton, M. B., Duez, M. D., et al. 2014, PhRvD, 90, 024026
Foucart, F., Desai, D., Brege, W., et al. 2017, CQGra, 34, 044002
Foucart, F., Duez, M. D., Kidder, L. E., et al. 2012, PhRvD, 85, 044015
Foucart, F., Duez, M. D., Kidder, L. E., et al. 2019, PhRvD, 99, 103025
Foucart, F., Duez, M. D., Kidder, L. E., & Teukolsky, S. A. 2011, PhRvD, 83, 024005
Foucart, F., Hinderer, T., & Nissanke, S. 2018, PhRvD, 98, 081501
Foucart, F., O'Connor, E., Roberts, L., et al. 2015, PhRvD, 91, 124021
Foucart, F., O'Connor, E., Roberts, L., et al. 2016, PhRvD, 94, 123016
Fragione, G. 2021, ApJL, 923, L2
Freiburghaus, C., Rosswog, S., & Thielemann, F. K. 1999, ApJL, 525, L121
Gompertz, B. P., Nicholl, M., Smith, J. C., et al. 2023, arXiv:2305.07582
Gottlieb, O., Issa, D., Jacquemin-Ide, J., et al. 2023, arXiv:2306.14947
Gottlieb, O., & Loeb, A. 2020, MNRAS, 493, 1753
Gottlieb, O., Nakar, E., & Piran, T. 2018a, MNRAS, 473, 576
Gottlieb, O., Nakar, E., Piran, T., & Hotokezaka, K. 2018b, MNRAS, 479, 588
Graham, M. J., Kulkarni, S. R., Bellm, E. C., et al. 2019, PASP, 131, 078001
Hamidani, H., & Ioka, K. 2023, MNRAS, 524, 4841
Hayashi, K., Fujibayashi, S., Kiuchi, K., et al. 2022a, PhRvD, 106, 023008
Hayashi, K., Kawaguchi, K., Kiuchi, K., Kyutoku, K., & Shibata, M. 2021, PhRvD, 103, 043007
Hayashi, K., Kiuchi, K., Kyutoku, K., Sekiguchi, Y., & Shibata, M. 2022b, arXiv:2211.07158

Hotokezaka, K., Wanajo, S., Tanaka, M., et al. 2016, MNRAS, 459, 35
Janka, H. T., Eberl, T., Ruffert, M., & Fryer, C. L. 1999, ApJL, 527, L39
Kasen, D., Badnell, N. R., & Barnes, J. 2013, ApJ, 774, 25
Kasliwal, M. M., Nakar, E., Singer, L. P., et al. 2017, Sci, 358, 1559
Kawaguchi, K., Kyutoku, K., Nakano, H., et al. 2015, PhRvD, 92, 024014
Kawaguchi, K., Kyutoku, K., Shibata, M., & Tanaka, M. 2016, ApJ, 825, 52
Kiuchi, K., Cerdá-Durán, P., Kyutoku, K., Sekiguchi, Y., & Shibata, M. 2015, PhRvD, 92, 124034
Korobkin, O., Rosswog, S., Arcones, A., & Winteler, C. 2012, MNRAS, 426, 1940
Kyutoku, K., Ioka, K., Okawa, H., Shibata, M., & Taniguchi, K. 2015, PhRvD, 92, 044028
Kyutoku, K., Ioka, K., & Shibata, M. 2013, PhRvD, 88, 041503
Kyutoku, K., Kiuchi, K., Sekiguchi, Y., Shibata, M., & Taniguchi, K. 2018, PhRvD, 97, 023009
Kyutoku, K., Okawa, H., Shibata, M., & Taniguchi, K. 2011, PhRvD, 84, 064018
Lazzati, D., Deich, A., Morsony, B. J., & Workman, J. C. 2017a, MNRAS, 471, 1652
Lazzati, D., López-Cámara, D., Cantiello, M., et al. 2017b, ApJL, 848, L6
Lazzati, D., Perna, R., Morsony, B. J., et al. 2018, PhRvL, 120, 241103
Liska, M. T. P., Chatterjee, K., Issa, D., et al. 2022, ApJS, 263, 26
LSST Science Collaboration, Abell, P. A., Allison, J., et al. 2009, arXiv:0912.0201
Margutti, R., & Chornock, R. 2021, ARA&A, 59, 155
Metzger, B. D. 2019, LRR, 23, 1
Metzger, B. D., Arcones, A., Quataert, E., & Martínez-Pinedo, G. 2010a, MNRAS, 402, 2771
Metzger, B. D., Bauswein, A., Goriely, S., & Kasen, D. 2015, MNRAS, 446, 1115
Metzger, B. D., Martínez-Pinedo, G., Darbha, S., et al. 2010b, MNRAS, 406, 2650
Mochkovitch, R., Hernanz, M., Isern, J., & Martin, X. 1993, Natur, 361, 236
Mooley, K. P., Nakar, E., Hotokezaka, K., et al. 2018a, Natur, 554, 207
Mooley, K. P., Deller, A. T., Gottlieb, O., et al. 2018b, Natur, 561, 355
Most, E. R., Papenfort, L. J., Tootle, S. D., & Rezzolla, L. 2021, MNRAS, 506, 3511
Nakar, E. 2020, PhR, 886, 1
Nakar, E., & Piran, T. 2017, ApJ, 834, 28
O'Connor, E. 2015, ApJS, 219, 24
Paczynski, B. 1991, AcA, 41, 257
Paschalidis, V., Ruiz, M., & Shapiro, S. L. 2015, ApJL, 806, L14
Perna, R., Lazzati, D., & Giacomazzo, B. 2016, ApJL, 821, L18
Piro, A. L., & Kollmeier, J. A. 2018, ApJ, 855, 103
Rantsiou, E., Kobayashi, S., Laguna, P., & Rasio, F. A. 2008, ApJ, 680, 1326
Rastinejad, J. C., Gompertz, B. P., Levan, A. J., et al. 2022, Natur, 612, 223
Rosswog, S. 2005, ApJ, 634, 1202
Ruiz, M., Shapiro, S. L., & Tsokaros, A. 2018, PhRvD, 98, 123017
Shibata, M., & Taniguchi, K. 2008, PhRvD, 77, 084015
Shibata, M., & Taniguchi, K. 2011, LRR, 14, 6
Shibata, M., & Uryū, K. 2006, PhRvD, 74, 121503
Shibata, M., & Uryū, K. 2007, CQGra, 24, S125
Shvartzvald, Y., Waxman, E., Gal-Yam, A., et al. 2023, arXiv:2304.14482
SpEC collaboration 2023, Spectral Einstein Code, https://www.black-holes.org/code/SpEC.html
Surman, R., McLaughlin, G. C., Ruffert, M., Janka, H. T., & Hix, W. R. 2008, ApJL, 679, L117
Tanaka, M., Hotokezaka, K., Kyutoku, K., et al. 2014, ApJ, 780, 31
Tanaka, M., Kato, D., Gaigalas, G., & Kawaguchi, K. 2020, MNRAS, 496, 1369
Timmes, F. X., & Swesty, F. D. 2000, ApJS, 126, 501
Wanajo, S., Fujibayashi, S., Hayashi, K., et al. 2022, arXiv:2212.04507
Wanajo, S., Sekiguchi, Y., Nishimura, N., et al. 2014, ApJL, 789, L39
Wu, Z., Ricigliano, G., Kashyap, R., Perego, A., & Radice, D. 2022, MNRAS, 512, 328
Yang, H., East, W. E., & Lehner, L. 2018, ApJ, 856, 110
Zhu, J.-P., Wu, S., Yang, Y.-P., et al. 2021, ApJ, 921, 156